Prediction of Structure-borne Noise Transmission Through Multiple/Multi-Dimensional Transfer Paths

R. Singh
Acoustics and Dynamics Laboratory, Dept. of Mechanical Engineering and Center for Automotive Research, The Ohio State University
650 Ackerman Road, Columbus, OH 43202, USA

S. Kim
Technical Center, The Goodyear Tire & Rubber Company
Akron, OH 44309-3531, USA

Abstract

Structure-borne noise within many practical systems is typically transmitted via multiple and/or multi-dimensional paths and thus the dynamic design of machines and mounts (or structural connections) requires a proper understanding of complex interactions that take place among visco-elastic mounts (or structural paths) and contiguous structures. Strengths and limitations of various quantification methods that rank order transfer paths are illustrated via two key examples. We employ the mobility method to synthesize the overall dynamic system over low and mid frequency regimes. First example (L structure) will illustrate the multi-dimensional effects, correlation of energy-based measures to sound radiation, and path coupling issues. Flexural motions of a beam structure are also analyzed to illustrate the spectral energies as well as the role of loss factor. Second, simplified vehicle system examples are considered. The analytical vehicle model consists of lumped models of powertrain, chassis and mounts, but the compliant vehicle body and enclosed acoustic cavity of irregular geometry are modeled using commercial codes. Typical quantification methods are further examined via a laboratory experimental system that consists of two chambers, which simulate the engine and passenger compartments respectively, and an emulated powertrain unit. Finally, some suggestions for further research will be made.

1 Introduction

Significant dynamic interations take place among multiple and/or multi-dimensional paths in many practical structures and machines. For example, in automotive systems the mounting systems of powertrain, chassis, exhaust components and many actuators transmit structure-borne noise to the passenger compartment. The effects of transfer paths and dynamic interactions among them, as well as with sources and receivers, on the overall noise performance are not well understood. Further, many elastic path elements exhibit multi-dimensional aspects beyond very low frequencies and thus the complexity of the problem increases. Identification of dominant path(s) in any system (or even a sub-system) is crucial for subsequent structural modifications or component selection in order to attenuate vibration and noise levels. However, a correct interpretation of the contributions of multiple paths is not straightforward, especially at low and mid frequencies. For example, conventional measures such as force and velocity transmissibilities may not be applicable to multi-dimensional problems since the associated transmissibility terms must be descibed using a matrix though the units of off-diagonal terms are not compatible [1]. Further, the existing methods of transfer path analysis, based on mobility or impedance formulation, seem to yield inconsistent

results in terms of rank ordering and their applications are cumbersome [1]. Vibratory energy (or power) analysis methods have been widely used to describe the dynamic behavior of structural and acoustic systems [1-6]. Both deterministic and statistical analyses have been employed to cover a broad range of frequencies even though some asymptotic methods are applicable only in the higher frequency regimes [6]. Further, the power flow through a path in a multiple path problem may inherently assume negative values, especially at low and mid frequencies, which would makes their interpretation unclear. Most power based methods [1-6] tend to focus on the dissipated power concepts although the determination of kinetic and potential energy spectra may be more appropriate to describe the dynamic behavior. Nevertheless, suitable methods that could truly characterize spectral kinetic and potential energy inputs to a vibratory system over a broad range of frequencies are, in general, not available [7].

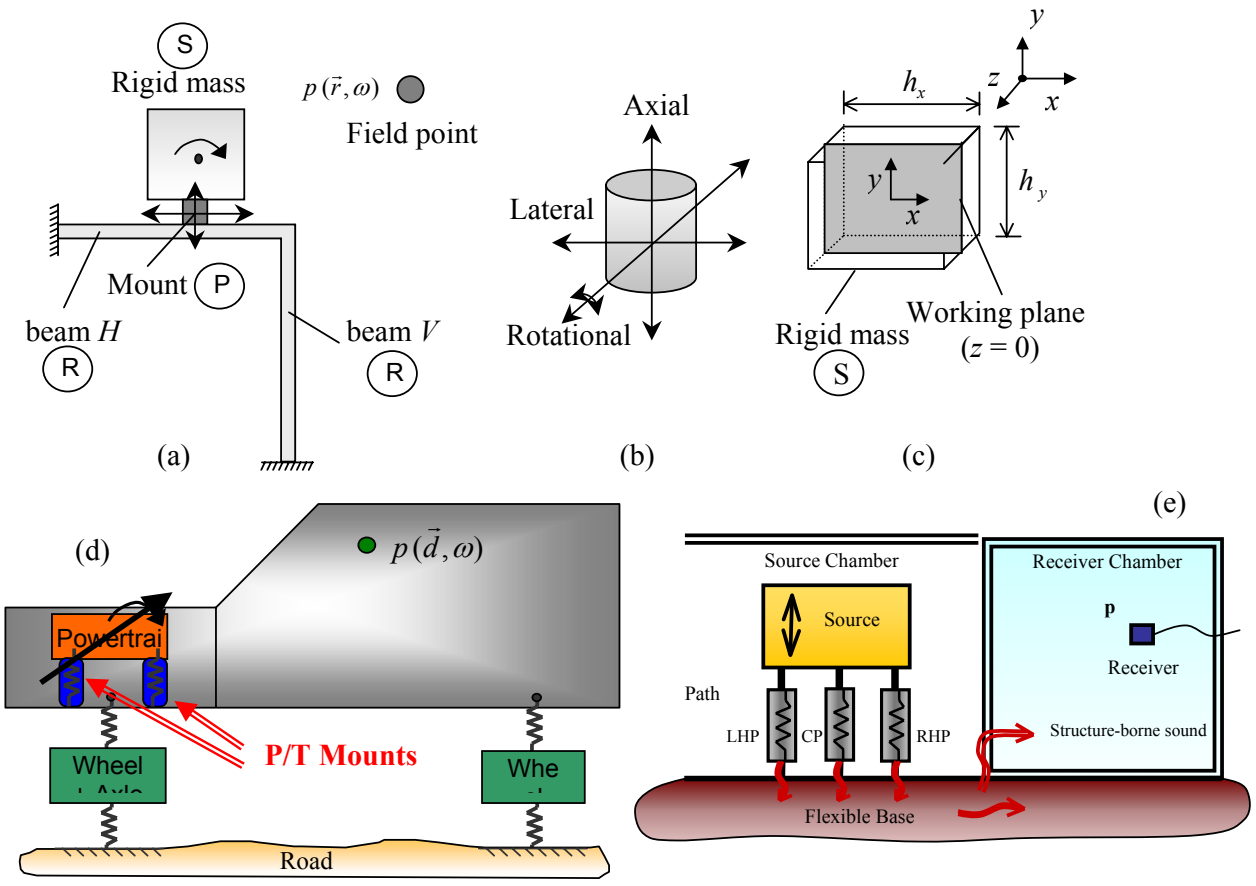

Figure 1. Examples cases. (a) System with an inverted 'L' beam receiver; (b) a cylindrical isolator with vibration transmission components; (c) isolator location [x , y , z] on the working plane of a cubic rigid body source: case 1 = [0, 0, 0]; case 2 = [$-h_x/2$, 0, 0]; here, S implies a simply supported edge and C denotes a clamped edge; (d) a simplified vehicle system with two mount paths; (e) schematic of an experimental source-path-receiver system that attempts to simulate a vehicle problem. In (e), left, center and right paths are connected to the source chamber structure via hard mountings and are denoted here as LHP, CP and RHP respectively.

Overall, the transfer path analysis and structure-borne noise transmission measures require further inquiries and research. To address some issues, we formulate a few research problems in Figure 1. Experimental and analytical systems with an inverted 'L' structure are investigated first and then simplified vehicle structures are employed to analyze the transfer path methods. The scope of this study is limited to the analysis of a linear time-invariant (LTI) system and the mobility synthesis method is employed to predict the harmonic response of the overall system. Both low and mid frequencies regimes are of interest. Specific objectives of the study, as reported in this article, include the following. 1. Investigate alternate transfer path analysis methods via laboratory experiments and analyses. 2. Examine energy-based measures for structure-bone noise transmission. 3. Propose a method to estimate the spectral energie inputs via the driving point transfer functions. We will provide a broad overview of each problem and then other references will be cited for more details.

2 Source characteristics of multi-dimensional structure-borne noise transmission

The effects of souce characteristics on structure-borne noise transmission is examined by calculating the sound pressure p at selected points in free field ($\vec{d}$) for the system of Figure 1(a). An inverted 'L' beam receiver is chosen as the chief radiating structure as it incorporates contributions from longitudinal and flexural structural motions. See Figure 2(a) for details of the sound radiation problems. Also, a detailed derivation of the sound field radiated from the 'L' beam can be found in our earlier article [1]. Calculated mean-square sound pressures (Ψ_p^2) are shown in Figure 2(b) for four alternate mount location cases of Figure 1(b). Horizontal beam is connected to the isolator at $3\ell_H/4$ from its clamped end. The field point is located at d = 1.0 m from the intersection of two beams, at 45^o from the outer surfaces of each beam, as shown in Figure 2(a). It is observed that sound pressures for cases 3 and 4 are almost the same but these are higher than those for cases 1 and 2. Also, the sound pressures are lowest among the cases considered when the isolator is attached to the mass center of a rigid body (case 1). Our calculation shows that the path rank orders (corresponding to four isolator locations) at different sound field observation points do not change, their spectral contents may slightly differ beyond 200 Hz. Refer to our article for results on sound pressures at other field locations [1].

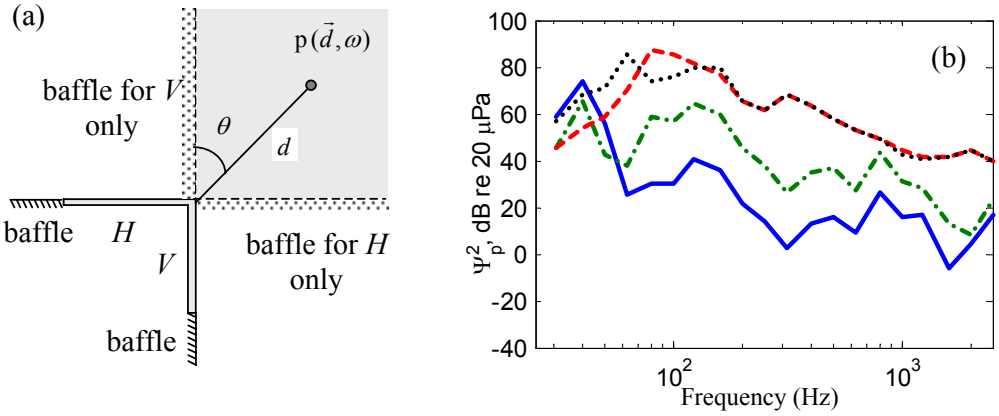

Figure 2. (a) Sound radiation from an inverted 'L' beam receiver; (b) Far field sound pressures radiated by the 'L' beam of Figure 2(a) at a field location (d = 1m, θ = 45^o). Key: ——— , mount location case 1; –·–·–·– , case 2; - - - - - - - -, case 3; ····· , case 4.

Similar to the inverted 'L' beam receiver, an inverted 'L' plate receiver, as shown in Figure 3, is employed to describe both in-plane and out-of plane motion transmissions to the receiver. A rubber isolator is located at either the center or edge of mass to realize different vibration isolation configurations. However, the mount location on the receiver side is unchanged. The field point for sound pressure measurements $p(\omega)$ is located at a distance of 0.2 m from the mating edge of two plates, at 45º from the outer surfaces. Measurement are conducted in an anechoic room under the sine sweep excitation (up to 3.0 kHz). In-phase and 180º out-of-phase forces (in *y* direction) are separately applied to the edges of the rigid source to simulate harmonic force (f_y) and moment (q_z) excitations at *G* respectively. The input forces with almost the same magnitudes and 180º (or 0º) phase difference are maintained throughout the experiments for moment (or force) excitation cases. Only the rotational free velocity of the source should exist for the moment excitation case when a mount is located at the center of the mass source. And, both translational and rotational free velocities occur when the isolator is placed at the edge of the rigid body source [1].
The mobilities of the inverted 'L' plate structure are obtained by using a commercial finite element (FEA) IDEAS code. Further, interfacial forces and moments between the isolator and receiver are calculated by synthesizing the mobilities of the inverted 'L' plate, source and isolator. Then, the plate velocity distribution (from FEA calculation) is provided to a commercial boundary element method (BEM) SYSNOISE code to predict the sound radiation. Individual sound fields generated by each plate for interfacial forces and moments are superimposed to determine the resultant sound pressures. Note that direct radiation from either source or isolator is not included in such calculations. Overall, sound pressure and velocity amplitudes are obtained by using a combined FEA and BEM methods.

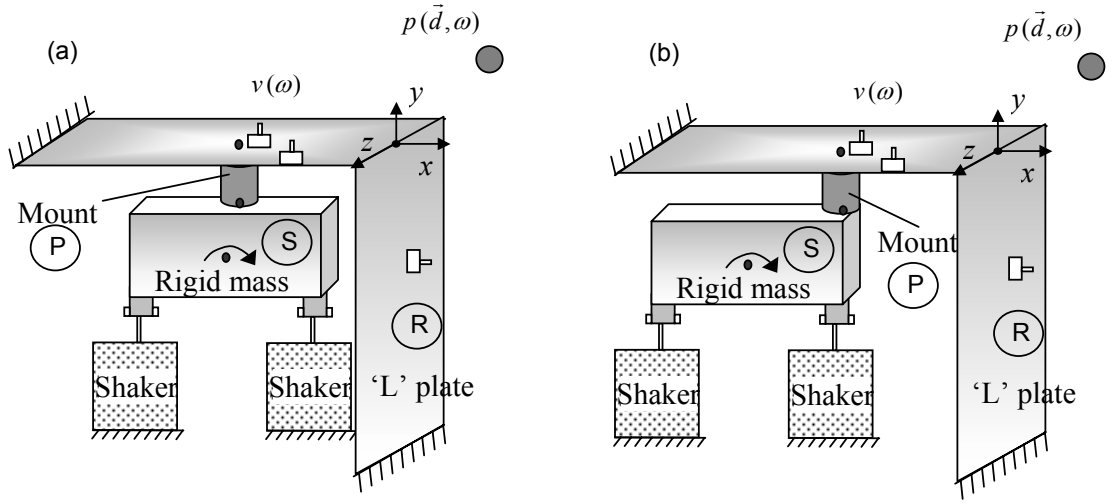

Figure 3. Experimental system with an inverted 'L' plate receiver, as excited by harmonic forces and moment. (a) System with free rotational velocity only; (b) system with both free translational and rotational velocities.

The effect of mount location is quantified in terms of insertion losses (*IL*) for sound pressure (*p*), vibration velocity (*v*) and radiation efficiency where

$$IL_{p_i} = 10\log_{10}\left(\frac{\Psi^2_{p_i,A}}{\Psi^2_{p_i,B}}\right), \text{dB};\ IL_{v_j} = 10\log_{10}\left(\frac{\Psi^2_{v_j,A}}{\Psi^2_{v_j,B}}\right), \text{dB};\ IL_{\Pi_{RAD}} = 10\log_{10}\left(\frac{\Pi_{RAD,A}}{\Pi_{RAD,B}}\right), \text{dB}. \quad (1a\text{-}c)$$

Here, p_i and v_j are sound pressure at acoustic field point *i* and velocity at receiver structure location *j* respectively. Further, '*A*' and '*B*' represent the system with an aluminum and rubber (or

polypropylene) isolator respectively. The IL_p and IL_v spectra are obtained from both experimental and computational studies. Results are given at the center frequencies of the 1/3 octave band, for both experimental and computational studies, in Figure 3. In this case, subscript '*A*' and '*B*' refer to the cases when the isolator is placed at the edge (A) and at the center of the mass (B) respectively. Further, the measured force inputs are used for computational studies. Resulting vibration and acoustic measures cannot be normalized with respect to their excitation forces since two different input forces are used. Both computational and experimental results show that all vibration and sound measures are significantly reduced when an isolator is moved from the edge to the mass center. However, measured IL_p spectra do not exhibit as much reduction as the ones computed beyond 500 Hz because the actual sound radiated from the receiver is lower than the shaker noise beyond 500 Hz, especially when a rubber isolator is located at the center of source, as shown in Figure 3(c). Further, IL_v spectra beyond 500 Hz are much higher than IL_p since measured IL_v are not contaminated by the shaker noise.

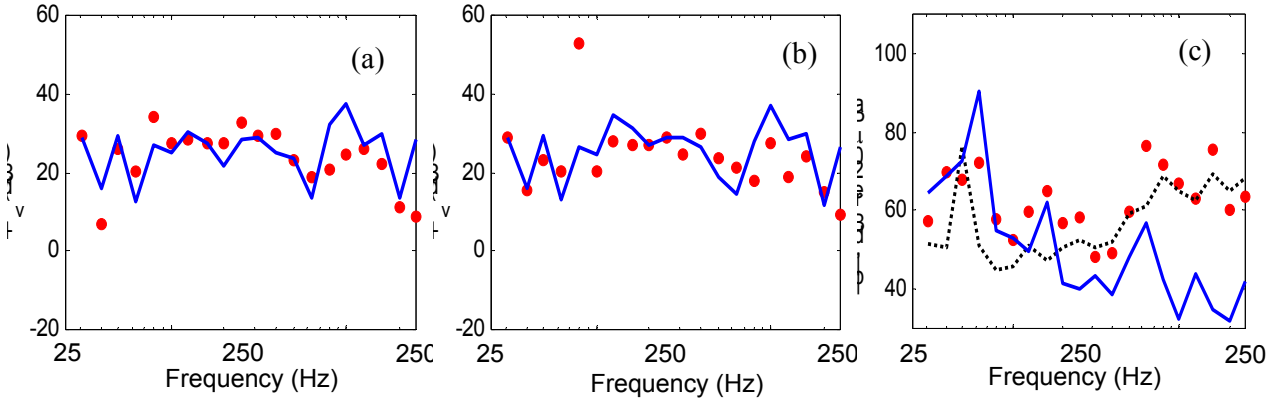

Figure 4. Vibration isolation measures for mount location studies, with a polypropylene isolator, given moment excitation. (a) Insertion loss (IL_p) of sound pressure at an acoustic field location; (b) insertion loss (IL_v) of velocity at a plate location; (c) absolute sound pressure levels at the acoustic field location. Key: ——— , calculated; ● , measured; ····· , background noise from shakers. Results are given in terms of 1/3 octave band center frequencies from 31.5 to 2500 Hz. Only the mean values within each bandwidth are plotted here.

3 Energy-based measures of structure-borne noise transmission

The energy-based vibrational measures are investigated. First, the vibration power is calculated for the 'L' beam structure of Figure 1(a) and is correlated to sound pressures that are radiated from the receiver structure. Figure 5 compares the insertion loss based on mean-squared sound pressures ($IL_{\psi_p^2,i-j}$) at a field point with the ones of vibration power input ($IL_{\Pi,i-j}$) to the 'L' beam for four isolator cases of Figure 1(c) given the moment excitation. Here, subscripts *i* and *j* denote mount cases as shown in Figure 1(d). Spectral averages of the insertion losses ($IL_{\psi_p^2,SAvg}$ and $IL_{\Pi,SAvg}$) are also compared in Figure 5. Figure 5 shows that the $IL_{\psi_p^2}$ spectra closely represent the IL_{Π} curves although some discrepancies between $IL_{\psi_p^2,4-1}$ and $IL_{\Pi,4-1}$ (cases 4 and 1) are observed. This suggests that $IL_{\psi_p^2,i-j}$ may not be equal to $IL_{\Pi,i-j}$ when systems *i* and *j* transmit different vibration components. Note that the rotational and axial components dominate the vibration transmission for cases 1 and 4

respectively. Therefore, in such cases, correlations between $IL_{\psi_p^2}$ and IL_{Π} could be enhanced by averaging sound pressures over the entire field.

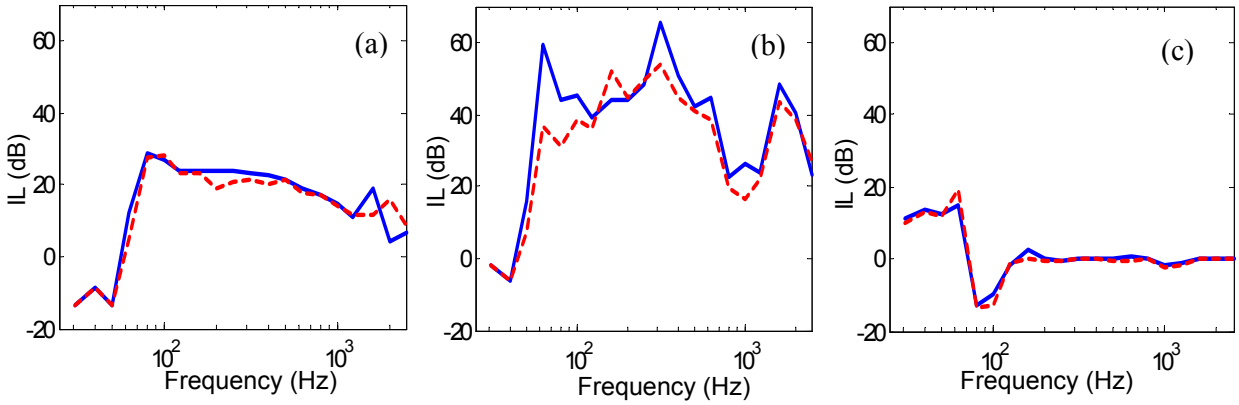

Figure 5. Insertion losses of mean square sound pressure ($IL_{\psi_p^2}$) and vibration power input (IL_{Π}) to the 'L' beam, given moment excitation, for four cases as shown in Figure 1(c). (a) $IL_{2\text{-}1}$ (case 2 - case 1) with spectral averages of $IL_{\psi_p^2,SAvg}$ = 14.3 dB, $IL_{\Pi,SAvg}$ = 13.5 dB; (b) $IL_{4\text{-}1}$ (case 4 - case 1) with $IL_{\psi_p^2,SAvg}$ = 35.9 dB, $IL_{\Pi,SAvg}$ = 31.5 dB; (c) $IL_{4\text{-}3}$ (case 4 - case 3) with $IL_{\psi_p^2,SAvg}$ = 1.0 dB, $IL_{\Pi,SAvg}$ = 1.4 dB. Key: ———, $IL_{\psi_p^2}$; - - - - - -, IL_{Π}. Here, subscript *SAvg* implies spectral average of corresponding insertion losses.

Next, the time-averaged kinetic, potential and dissipated energy spectra are calculated and the energy input measures are compared using the insertion losses (IL) spectra for the system of Figure 6(b). Note that the vibration power represents the rate of energy change and it is directly related to the time-averaged dissipated energy by a multiplication of circular frequency for the harmonic case. Three spectrally-varying insertion losses of time-averaged kinetic, potential and dissipated energies are defined here as follows:

$$IL(\overline{E}_m;\omega) = \frac{\overline{E}_m \text{ with } \eta_2}{\overline{E}_m \text{ with } \eta_1}, \quad IL(\overline{E}_k;\omega) = \frac{\overline{E}_k \text{ with } \eta_2}{\overline{E}_k \text{ with } \eta_1}, \quad IL(\overline{E}_d;\omega) = \frac{\overline{E}_d \text{ with } \eta_2}{\overline{E}_d \text{ with } \eta_1}. \qquad \text{(2a-c)}$$

Insertion losses of (2a-c) are calculated for the clamped beam of Figure 6 when equal forces are applied and results are shown in Figure 7 for flexural motions. Refer to [7] for a detailed derivation of energy quantities. Figure 7 shows that the $IL(\overline{E}_m)$ values approach the ratio of two alternate system loss factors at higher frequencies. However, it is observed that $IL(\overline{E}_d)$ converges to unity. Essentially, $\overline{E}_d$ describes no distinction between two systems at higher frequencies, unlike $\overline{E}_m$. This implies that $\overline{E}_m$ with a highly damped system is lower than the one with a lightly damped system but $\overline{E}_d$ with higher damping also increases due to higher η and the two $\overline{E}_d$ values remain the same at higher frequencies. Hence, one can expect that the application of high damping may not lessen the role of dissipated energy although the kinetic energy input is significantly reduced at higher frequencies. Conversely, Figure 7 shows that $IL(\overline{E}_m)$ is unity and $IL(\overline{E}_d)$ displays the inverse of the ratio of loss factors at very low frequencies. This indicates that the application of high damping increases $\overline{E}_d$ but $\overline{E}_m$ remains the same at lower frequencies. Further, $IL(\overline{E}_m)$ and $IL(\overline{E}_k)$

are found to be very close each other at all frequencies. Finally, the ratio of $IL(\overline{E}_k)$ and $IL(\overline{E}_d)$ is the ratio of damping loss factors, as expected.

(a) (b)

Figure 6. Clamped-free beam given a harmonic force excitation at the free edge. (a) Under longitudinal (x) excitation; (b) under flexural (y) excitation.

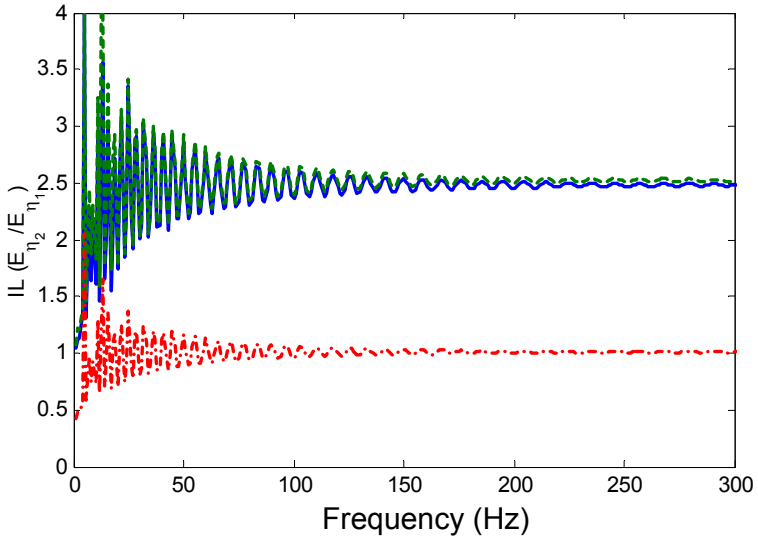

Figure 7. Insertion loss ($IL(\overline{E})$) spectra of time-averaged energy for flexural motions of a clamped-free beam of Figure 6(b) given a force excitation at the free end. Key: ——— , $IL(\overline{E}_m)$; — · — · , $IL(\overline{E}_k)$, - - - - - , $IL(\overline{E}_d)$.

Next, the spectral energy inputs to a structure are characterized by using only the driving point impedances or mobilities. In this article, two alternate characterization methods are examined and these are referred to as Methods 1 and 2. Method 1, that has been originally proposed by Bobrovnitskii and Korotkov [8], is based on the following equations for impedance and mobility formulation respectively where $\mathbf{Z}$, $\mathbf{M}$, $\mathbf{V}$ and $\mathbf{F}$ are the impedance, mobility matrices, velocity and force vectors respectively at any frequency:

$$\hat{\overline{E}}_{1Z,m} = \mathbf{V}_{\mathrm{D}}^{*\mathrm{T}}\ \mathrm{Im}[\mathbf{Z}_{\mathrm{D}}/\omega + \partial\mathbf{Z}_{\mathrm{D}}/\partial\omega]\ \mathbf{V}_{\mathrm{D}}/4\,, \quad \hat{\overline{E}}_{1Z,k} = -\mathbf{V}_{\mathrm{D}}^{*\mathrm{T}}\ \mathrm{Im}[\mathbf{Z}_{\mathrm{D}}/\omega - \partial\mathbf{Z}_{\mathrm{D}}/\partial\omega]\ \mathbf{V}_{\mathrm{D}}/4\,. \quad \text{(3a-b)}$$

$$\hat{\overline{E}}_{1M,m} = \mathbf{F}_{\mathrm{D}}^{*\mathrm{T}}\ \mathrm{Im}[\mathbf{M}_{\mathrm{D}}/\omega + \partial\mathbf{M}_{\mathrm{D}}/\partial\omega]\ \mathbf{F}_{\mathrm{D}}/4\,, \quad \hat{\overline{E}}_{1M,k} = -\mathbf{F}_{\mathrm{D}}^{*\mathrm{T}}\ \mathrm{Im}[\mathbf{M}_{\mathrm{D}}/\omega - \partial\mathbf{M}_{\mathrm{D}}/\partial\omega]\ \mathbf{F}_{\mathrm{D}}/4\,. \quad \text{(3c-d)}$$

Here, $\overline{E}_m$, $\overline{E}_k$ and $\overline{E}_d$ represent the time-averaged kinetic, potential and dissipated energies respectively. Further, the superscript ^ denotes the estimate and subscript D implies that it is at the driving point. Method 1 further refines the estimates from equations (3a-d) by compensating limitations of the original method. Refer to [8] and [9] for further details of refined and original characterization methods by Bobrovnitskii et al. To overcome the deficiencies of Method 1, we propose Method 2 that employs the spectral energy concept and characterizes the time-averaged energies as follows:

$$\hat{\tilde{E}}_{2m} = \left|\tilde{E}_m\right| \approx \bar{E}_m, \qquad \tilde{E}_m = \frac{1}{4j} v_1 \left[\frac{z_{D11}}{\omega} + \frac{\partial z_{D11}}{\partial \omega}\right] v_1, \tag{4a-b}$$

$$\hat{\tilde{E}}_{2k} = \left|\tilde{E}_k\right| \approx \bar{E}_k, \qquad \tilde{E}_k \approx \frac{1}{4j} v_1 \left[\frac{z_{D11}}{\omega} - \frac{\partial z_{D11}}{\partial \omega}\right] v_1, \tag{4c-d}$$

Refer to our recent article for more analytical details on Method 2 [7]. To illustrate the concepts, both energy characterization methods are compared next. The estimates of sum of time-averaged kinetic and potential energies from Method 2 are calculated for longitudinal motions of Figure 6(a) and are compared with the ones from Method 1 in Figure 8(a, b). Both Methods 1 and 2 come very close to the exact kinetic and potential energies but the deviations increase as damping and/or frequency increase. Further, Method 2 produces a most consistent prediction using either impedance or mobility formulation while Method 1 exhibits different results from impedance and mobility. Furthermore, many spurious peaks are observed in Figure 8(a, b) for the estimates from Method 1.

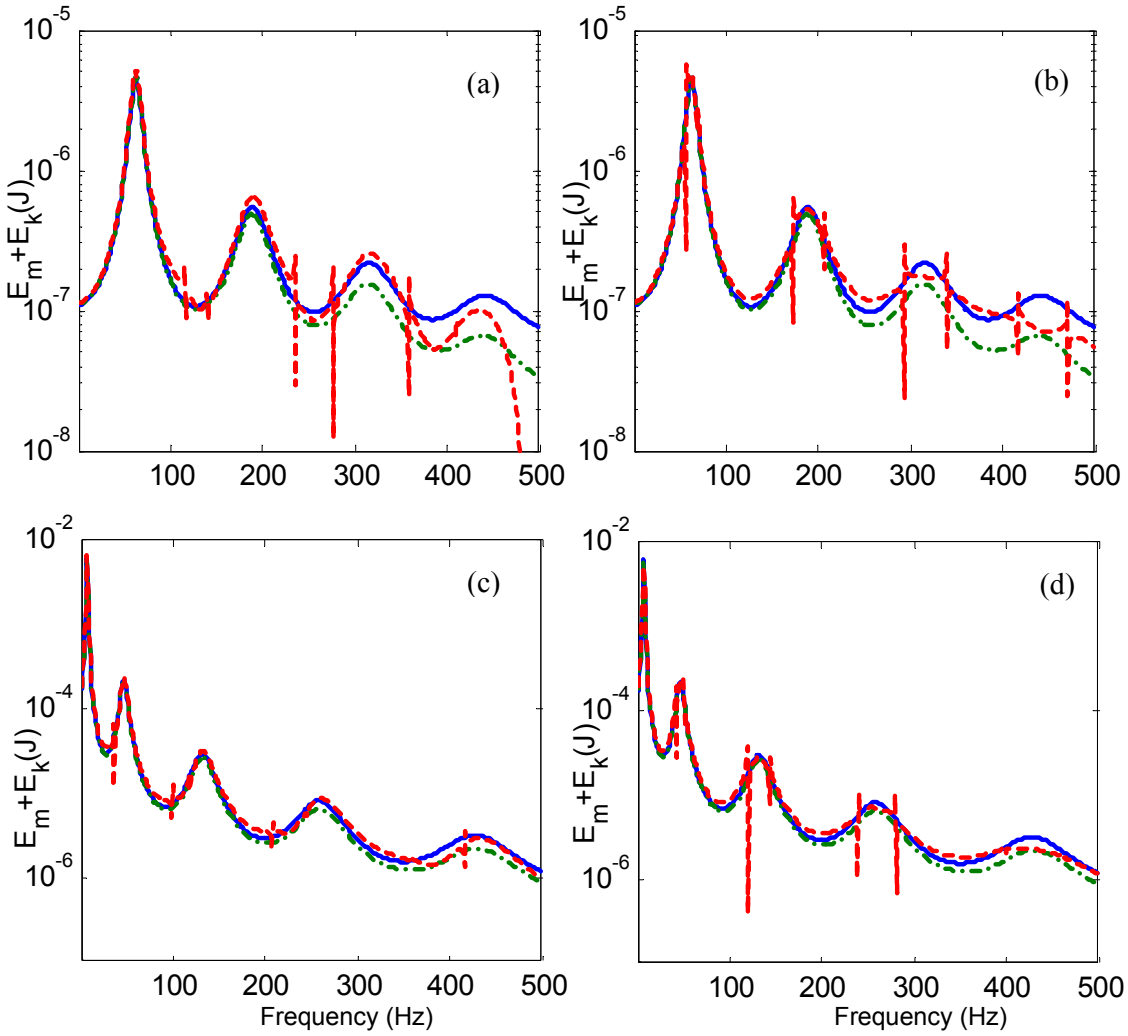

Figure 8. Sum of time-averaged kinetic and potential energies of a clamped-free beam (η=0.2) given harmonic force excitation at the free end. (a) Longitudinal motions of Figure 6(a) with impedance; (b) longitudinal motions with mobility; (c) flexural motions of Figure 6(b) with impedance; (d) flexural motions with mobility. Key: ——, Exact; — · — · —, Method 2, - - - - -, Method 1.

Figure 8(a, b) also shows that $\overline{E}_m + \overline{E}_k$ from Method 1 (with impedance) deviates more around 450 Hz and yields negative values at the end of frequency band. Such a magnified deviation results from the odd number of zero crossing points within the frequency band that the original Method 1 [8] utilizes. Note that the numerical modeling and compensation procedures of Method 1 require pairs of the zero crossing points [9]. Calculated results for the flexural motions of the finite beam of Figure 6(b) are shown in Figure 8(c, d). Similar to the longitudinal motion case, both $\hat{\overline{E}}_{2m} + \hat{\overline{E}}_{2k}$ and $\hat{\overline{E}}_{3m} + \hat{\overline{E}}_{3k}$ estimates are close to the exact values but the deviations between the estimates and the exact ones are again observed as the frequency and/or damping increase. Like the previous case, Figure 8(c, d) shows that $\hat{\overline{E}}_{2m} + \hat{\overline{E}}_{2k}$ produces erroneous peaks and the mobility and impedance formulations yield different results. However, Method 2 yields the same results from impedance and mobility, like the longitudinal motions [7].

4 Quantification of structure-borne noise transfer paths

4.1 Analytical model of simplified vehicle system

The simplified vehicle system of Figure 1(d) is employed to examine the powertrain mounts paths. Like the system with an inverted 'L' structure, mobilities of each component of Figure 1(c) are analytically or computationally obtained, and then the mobility synthesis method is employed to predict the harmonic response of the overall system; the procedure is based on the formulation that was reported in our earlier article [4]. For example, the simplified vehicle body is modeled by a commercial FEA code to compute the velocity field of the body structure and the sound field inside cabin is obtained by a commeral BEM code given the velocity distribution of passenger compartment walls only. Typical FEA and BEM models are shown in Figure 9(a) and (b) respectively. Lumped models are used for other components such as powertrain, chassis and wheel etc. Harmonic moment excitation is applied to the powertrain, up to 1 kHz and an attempt is made to quantify these paths in this study. Sound pressure at a point in a passenger cabin is described as two alternate representations as follows where subscript M and Z denote mobility and impedance respectively:

$$p(\omega) = \sum_i [p_{Z,i}] = \sum_i \left[\frac{p}{V_i}\right] V_i \,, \qquad p(\omega) = \sum_i [p_{M,i}] = \sum_i \left[\frac{p}{F_i}\right] F_i \,. \tag{5a, b}$$

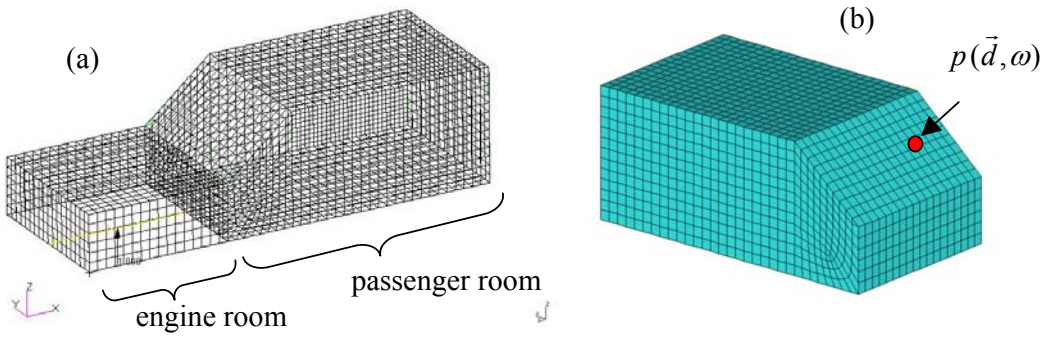

Figure 9. Schematic of the simplified vehicle system.

Here, equations 5(a) and (b) are referred here as mobility and impedance formulations as they are based on free and blocked boundary conditions respectively. In order to compare the partial sound pressures based on the impedance and mobility formulations, the following relative sound pressure (Δp) is defined where subscripts i and j are the path indices.

$$\Delta p_{i-j} = 20\log_{10}\left(\frac{|p_i|}{|p_j|}\right), \quad i, j = 1, 2, 3. \tag{6}$$

Figure 10(a) shows that mobility and impedance formulations yield somewhat different results depending on the frequencies. A vectorial representation of the partial pressures are also shown in Figure 10(b) and exhibits rather clear distinction between those two formulations which may indicate two alternate interpretations in terms of path rank ordering. However, note that total sound pressure, which is depicted by a solid red arrow in Figure 10(b), should be equal for both formulations. Hence, one can not judge which formulation presents a more accurate path rank order.

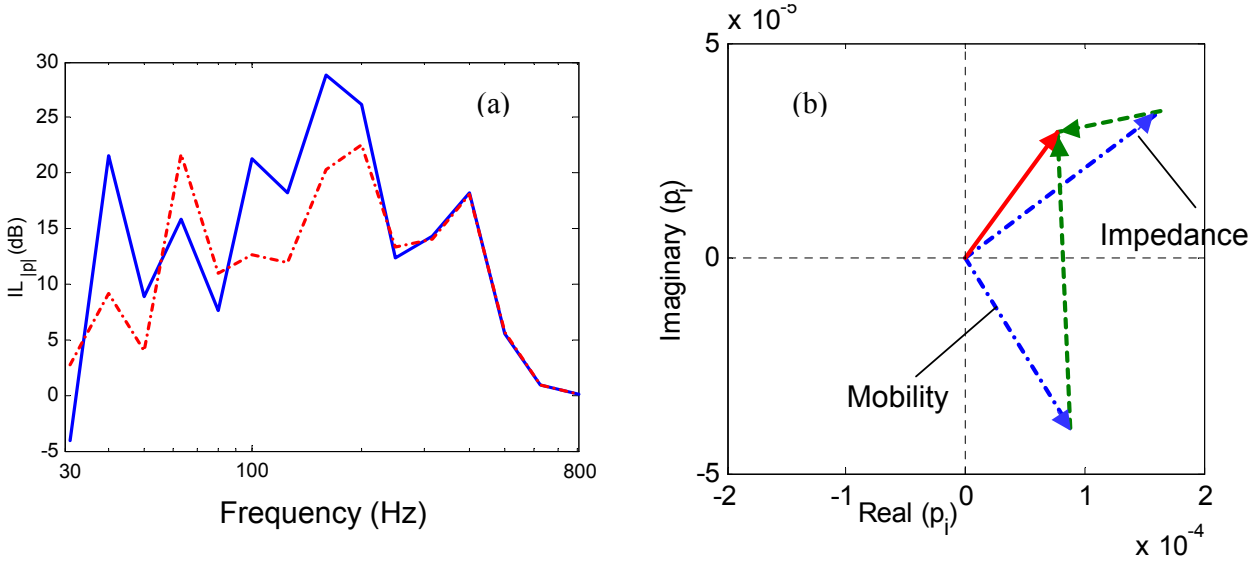

Figure 10. Transfer path measures from front and rear mounts of Figure 1(d). (a) Insertion loss of partial sound pressures; Key: ——, free boundary for powertrain (mobility formulation); — · —, blocked boundary for powertrain (impedance formulation); (b) vectorial representation of partial sound pressures at 80 Hz; Key: ——— , total sound pressure; — · —, mobility formulation; – – –, impedance formulation.

4.2 Experimental transfer path analysis

Next, transfer paths are quantified by using an experimental system that consists of source and receiver chambers. These two chambers simulate the engine and passenger compartments, respectively, as depicted in Figure 11(a). A motor and an air pump are fixed on a T-shape plate, as shown in Figure 11(b), which emulate a powertrain unit. Both motor and pump act as the vibration sources, and each source can be operated separately, and thus they are uncorrelated. The powertrain unit is mounted on the base of the source chamber by three hard mounts, which constitute the main structure-borne transmission paths, and the structure-borne noise is finally transmitted into the receiver chamber as shown in Figure 11(a). Refer to [10] for detailed experimental procedures.

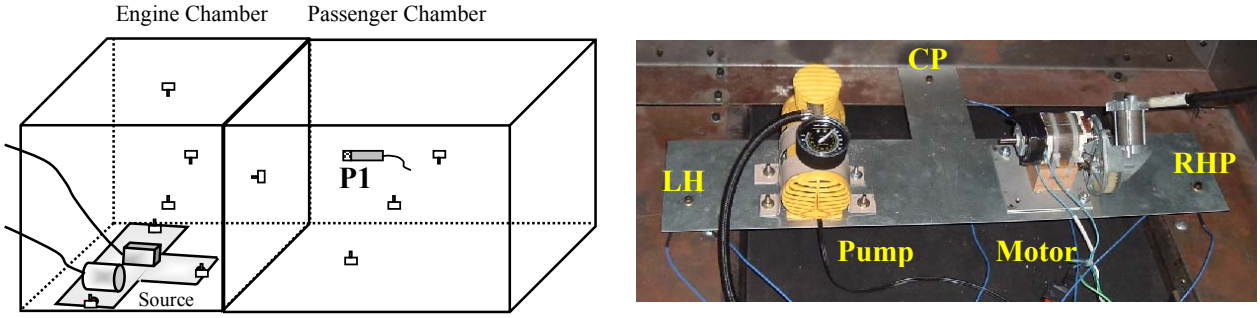

(a) (b)

Figure 11. (a) Schematic of source-receiver chamber system with three hard mounting paths; (b) emulated powertrain unit that consists of an air pump, a motor and a T-shaped base plate.

Four alternate schemes are employed to rank order the structural paths in terms of the partial sound pressure components. First, consider the mobility and impedance formulations, which represent free and blocked boundary conditions respectively. Each is evaluated in terms of forces or velocities. The four formulations are written as follows where p is the sound pressure in the receiver room at a given frequency and subscripts M, Z, F and V represent mobility formulation, impedance formulation, measured force and measured velocity respectively. Moreover, subscripts m and e denote measured and estimated quantities respectively, and subscript *i* indicates the structural path component of interest.

$$p_{FM}(\omega)=\left[\frac{\mathbf{p}}{\mathbf{F}}\right]_{1\times 3}[\mathbf{F_m}]_{3\times 1}=\sum_i\left[p_{FM,i}\right]=\sum_i\left[\frac{p}{F_i}\right]F_{mi},\quad p_{FZ}(\omega)=\left[\frac{\mathbf{p}}{\mathbf{V}}\right]_{1\times 3}[\mathbf{V_e}]_{3\times 1}=\sum_i\left[p_{FZ,i}\right]=\sum_i\left[\frac{p}{V_i}\right]V_{ei}\ , \quad \text{(7a-b)}$$

$$p_{VM}(\omega)=\left[\frac{\mathbf{p}}{\mathbf{F}}\right]_{1\times 3}[\mathbf{F_e}]_{3\times 1}=\sum_i\left[p_{VM,i}\right]=\sum_i\left[\frac{p}{F_i}\right]F_{ei},\quad p_{VZ}(\omega)=\left[\frac{\mathbf{p}}{\mathbf{V}}\right]_{1\times 3}[\mathbf{V_m}]_{3\times 1}=\sum_i\left[p_{VZ,i}\right]=\sum_i\left[\frac{p}{V_i}\right]V_{mi}\ . \quad \text{(7c-d)}$$

Further, we define $[\mathbf{p/V}]_{1\times 3}$ and $[\mathbf{v}_e]_{3\times 1}$ as follows by using the measured acoustic frequency function $[\mathbf{p/F}]_{1\times 3}$:

$$\left[\frac{\mathbf{p}}{\mathbf{V}}\right]_{1\times 3}=\left[\frac{\mathbf{p}}{\mathbf{F}}\right]_{1\times 3}[\mathbf{M}]^{-1}_{3\times 3},\qquad [\mathbf{V_e}]_{3\times 1}=[\mathbf{M}]_{3\times 3}[\mathbf{F_m}]_{3\times 1}. \quad \text{(8a-b)}$$

Note that $p_{FM}(\omega)=p_{FZ}(\omega)$ and $p_{VM}(\omega)=p_{VZ}(\omega)$ although their partial components are not necessarily the same such as $p_{FM,i}\neq p_{FZ,i}$ and so on. Sound pressures in the receiver room are estimated in Figure 12 via measured force and velocity formulations of equations (7). These estimations are compared with the direct measurements of sound pressures. Overall, the estimated sound pressures match well with the measured levels over a broad range of frequencies. However, the sound pressure that is estimated via the measured force shows a relatively large deviation from the direct measurements up to 300 Hz.

Rank orders of structural paths based on measured forces and velocities are shown in Figure 13. Measured forces show that right path is the weakest and left and center paths are equally dominant, as shown in Figure 13(a). Unlike the rank order based on interfacial forces, the order of dominance is more clear in the velocity spectra over a broad range of frequencies. Figure 13(b) shows that velocity is maximum at left path and center path is the weakest.

Figure 14 shows the partial sound pressure spectra that are estimated by the mobility method with the measured path forces. Overall, the center path is dominant in the partial sound pressure spectra

as shown in Figure 14(a). Partial sound pressures that are estimated with the measured velocities are also shown in Figure 14(b). Unlike the ones with measured forces of Figure 14(a), the center path is not as dominant. And, the right and center paths are somewhat the same up to 300 Hz, as shown in Figure 14(b).

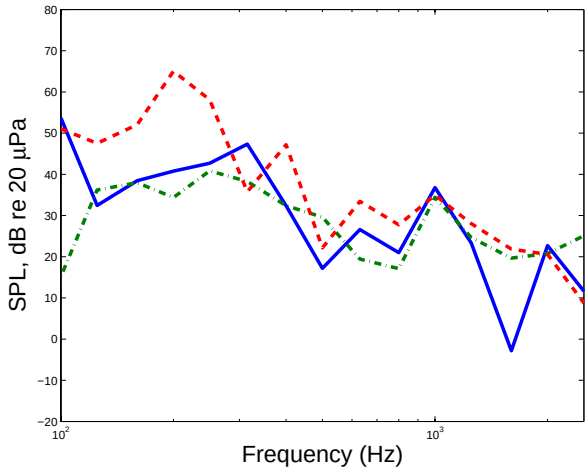

Figure 12. Estimated sound pressure (SPL) in the receiver room. Key: ——, measured SPL; — · —, estimated SPL ($p_{FM} = p_{FZ}$) using measured velocity; — — —, estimated SPL ($p_{VM} = p_{VZ}$) using measured force.

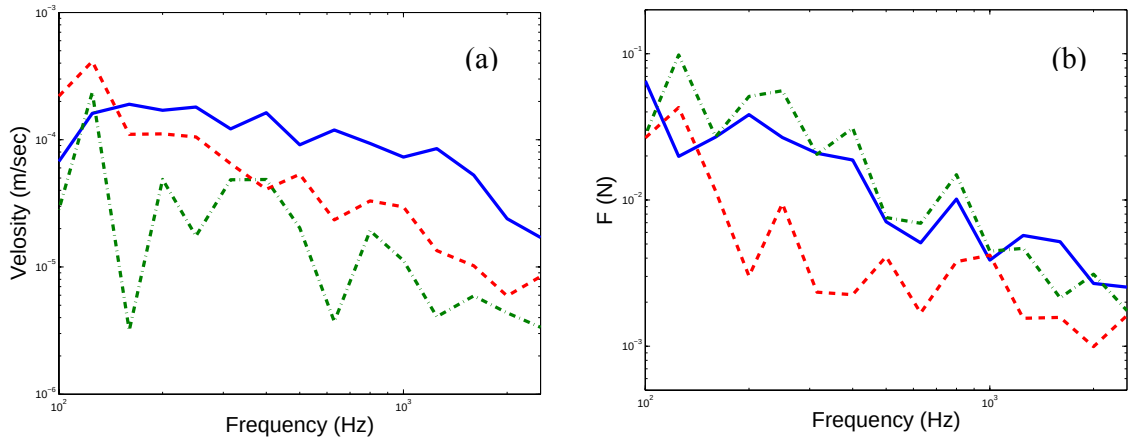

Figure 13. Measured interfacial force (a) and velocity (b) spectra at paths. Key: ——, left path; — · — ·, center path; — — —, right path.

Like the previous analytical model, relative sound pressures are calculated and results are shown in Figure 15. Relative sound pressures of Figure 15 show that the rank order of paths and their relative strengths are formulation-dependent. For example, the right path is dominant in the impedance method around 700 Hz but the partial sound pressure of the left path is larger than the one of right path in the mobility representation at that frequency, as shown in Figure 15(c). However, note that total sound pressures of Figure 14 from either the mobility or impedance methods should be identical.

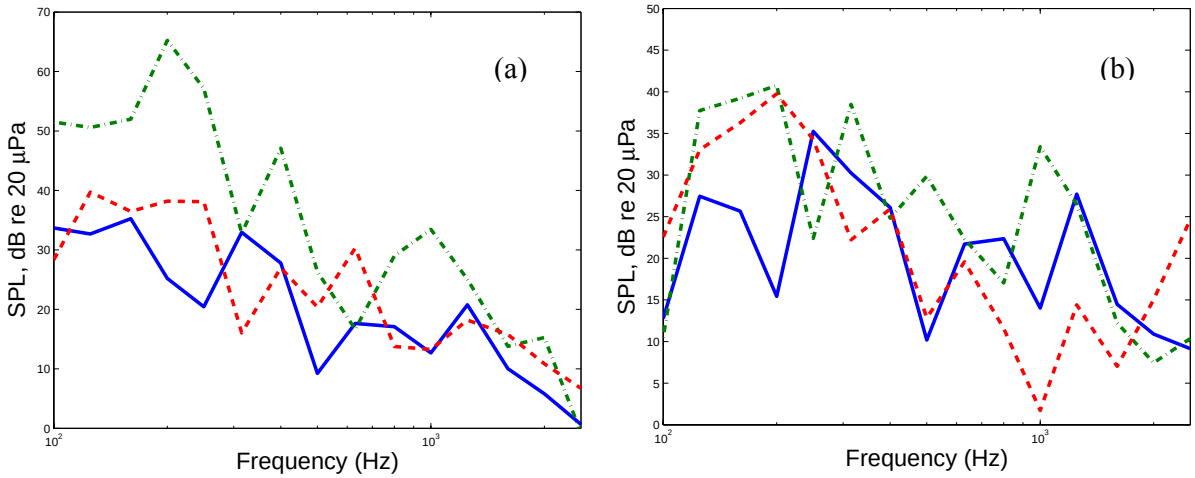

Figure 14. Estimated partial sound pressures via the mobility method. (a) Given measured forces; (b) given measured velocities. Key: ——, left path; — · — ·, center path; — — —, right path.

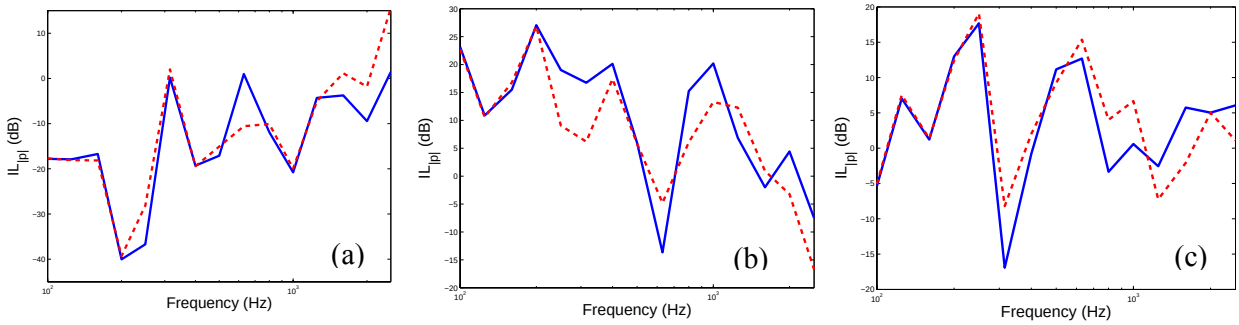

Figure 15. Relative partial sound pressures. (a) Δp_{LHP-CP}; (b) Δp_{CP-RHP}; (c) $\Delta p_{RHP-LHP}$. Key: ——, mobility method; — — —, impedance method.

Similar to the analytical system, sound pressure components are next represented in a vectorial form in Figure 16 for both mobility and impedance formulations. Figure 16 illustrates that the sound pressure components from the three paths constitute the total (measured) sound pressure in different ways for the mobility and impedance methods. Hence, Figure 16 further reveals that the descriptions of path contributions to the resulting partial pressures depend on the boundary condition formulation, such as the blocked and free conditions that are shown in Figure 16(a) and (b) respectively. Furthermore, there may be an infinite number of vectorial representations to describe the same sound pressure spectrum at an observation point in the passenger cabin. Nonetheless, it appears that the mobility type formulation is (and should be) preferred in practice since the free boundary conditions can be easily implemented in the labortaory. Further note that total sound pressure is the same (as it should) for those alternate representations; see the red lines in Figures 16(a) and (b).

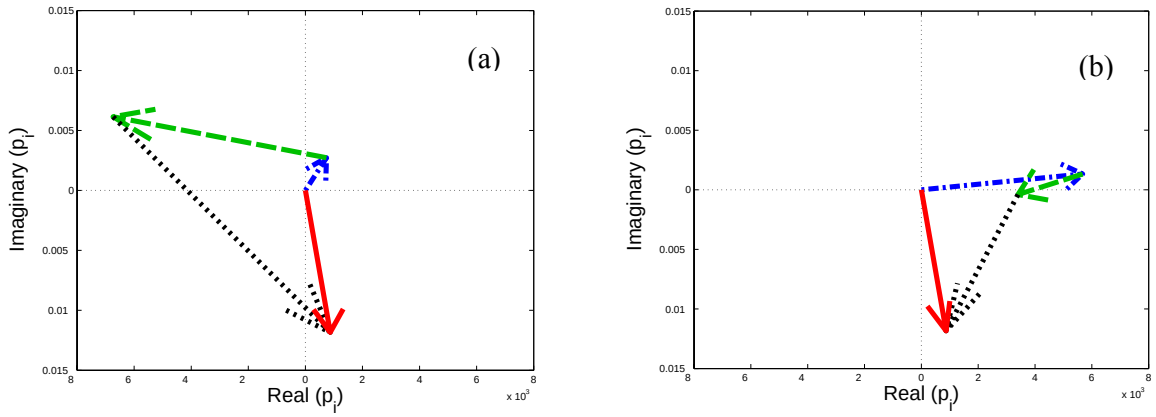

Figure 16. Vectorial representations of partial sound pressures at 227 Hz, estimated using measured forces. (a) impedance method; (b) mobility method. Key: ——, total sound pressure, – – –, from left path; –·–·–, from center path; ·····, from right path.

Next, vibration power spectra for three structural paths are obtained by using measured forces and velocities of Figure 13 and results are shown in Figure 17(a) and (b) for total power and power components respectively. The power components of Figure 17(b) show that the right path is more dominant from 100 to 300 Hz. Further, Figure 17(b) shows that Π at the center path exhibits negative values over a wide range of frequencies, say from 100 to 1000 Hz. Note that the power flow through any path may be negative for a multiple paths case and thus an interpretation of the negative power flow is somewhat cumbersome. Nonetheless, the total power should be positive at all frequencies as shown in Figure 17(a). Care must be however exercised since the total power could be negative for an experimental system especially when some degrees of freedom (say the rotational directions) are not taken into account. Refer to [1] for further explanation.

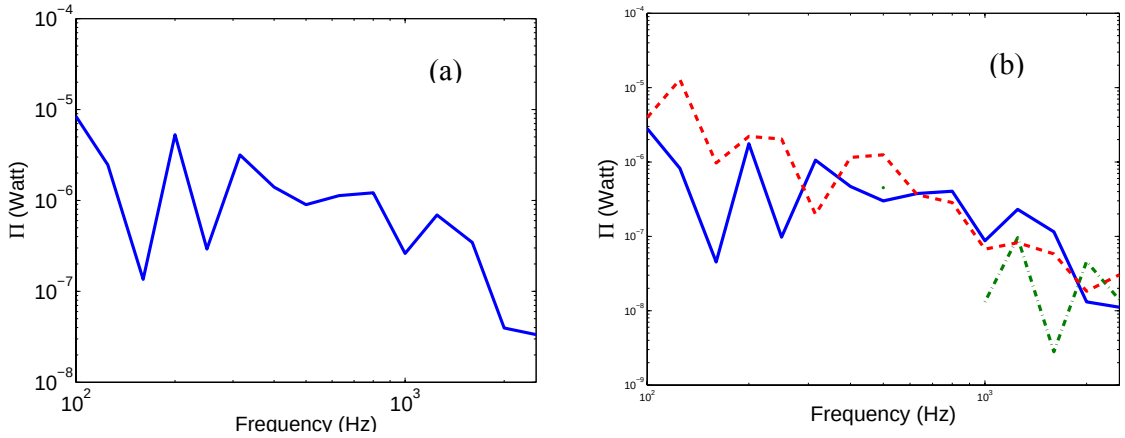

Figure 17. Power flow (W) through structural paths. (a) Total power flow through all paths; (b) power flow through individual paths. Key: (a) ——, total power flow; (b) ——, from left path; –·–·–, from center path; – – –, from right path. Negative power values are not shown here.

5 Conclusion

5.1 Summary

In our work, alternate structure-borne noise measures are analtically and experimentally examined by using several examples. Vibration powers, that are transmitted to an inverted 'L' structure receiver, are calculated and are coorelated with sound radiated from the receiver. Sound measurements and predictions for the inverted 'L' plate demonstrate that a rank order based on free field sound pressures, at a properly selected point, could be regarded as a measure of the vibration power transmitted to the receiver. The effects of source characteristics on the structure-borne noise transmission through a multi-dimensional isolation system are also examined via systems with the 'L' structure receiver. Measured and predicted insertion loss spectra show that vibration transmitted to a receiver is indeed significantly reduced when the chosen isolator location minimizes the free translational velocity of the source. Path quantification measures are also experimentally and analytically investigated via simplified vehicle systems over low and mid frequency regimes. It is shown that the rank order of paths and their relative strengths are formulation-dependent. Further, vibration power is employed to assess the noise paths but the negative values of measured powers are observed over a wide range of frequencies and interpretations of such negative power quantities are unclear. Finally, a new formulation has been proposed for the spectral energy characterization based on a correct interpretation of the driving point mobilities or impedances. The proposed method is insensitive to the driving point mobility or impedance formulations, and it yields consistent results, unlike the existing methods. However, our method still shows some discrepancies near resonances as the structural loss factor is increased.

5.2 Research issues

Several efforts have been made to quantify the contribution of parallel paths to vibration transmission from a harmonic source to a receiver. However, a more appropriate quantification of path and/or source strength is still required. In particular, dynamic interactions between source(s) and paths would need further investigation, especially in the presence of multi-dimensional and multiple paths and compliant source(s). In conjunction with the transfer path quantification issue, coupling phenomena need to be properly interpreted in order to develop efficient transfer path measures. Most importantly, a formulation-independent path quantifier is essential for further development of dynamic design schemes.

One method has been developed to better characterize spectral energy quantities that are transmitted to receiver structures. However, further work is also necessary to improve the methodology. For example, one needs to develop the energy characterization schemes when multiple harmonic inputs are applied to a vibratory system, especially for complex structures. In relation to such energy-based measures, an appropriate interpretation of energy flow is also required to predict the contributions from paths, particularly at low and mid frequencies. All of the above considerations have assumed that the governing system is linear, and therefore some work on the dynamics of non-linear paths (such as those associated with elastomeric or hydro-elastic mounts) should be examined in future investigations. Finally, we need to develop design principles for reduced structure-borne noise, especially for "real life" systems such as the ground vehicle structures.

Acknowledgement

The Center for Automotive Research Industrial Consortium at The Ohio State University is gratefully acknowledged for supporting this research.

References

[1] R. Singh and S. Kim, Journal of Sound and Vibration, 'Examination of Multi-Dimensional Vibration Isolation Measures and Their Correlation to Sound Radiation over a Broad Frequency Range', **262**(3), 419-455, (2003).

[2] L. Cremer and M. Heckle, Structure-Borne Sound: Structural Vibrations and Sound Radiation at Audio Frequencies (Springer-Verlag , New York, 1973).

[3] J. L. Wohlever and R. J. Bernhard, Journal of Sound and Vibration, 'Mechanical Energy Flow Models of Rods and Beams', **153**(1), 1-19, (1992).

[4] S. Kim and R. Singh, Journal of Sound and Vibration, 'Vibration Transmission Through an Isolator Modeled by Continuous System Theory', **248**(5), 925-953, (2001).

[5] T. E. Rook and R. Singh, Noise Control Engineering Journal, 'Mobility Analysis of Structure-borne Noise Power Flow through Bearings in Gearbox-like Structures', **44**(2), 69-78, (1996).

[6] R. H. Lyon and R. G. Dejong, Theory and Application of Statistical Energy Analysis (Butterworth-Heinemann, Boston, 1995).

[7] S. Kim and R. Singh, Submitted to Journal of Sound and Vibration, 'Alternate Methods for Characterizing Spectral Energy Inputs Based Only on Driving Point Mobilities or Impedances', accepted subject to revisions (2004).

[8] Y. I. Bobrovnitskii and M. P. Korotkov, Journal of Sound and Vibration, 'Improved Estimates for the Energy Characteristics of a Vibrating Elastic Structure via the Input Impedance and Mobility: Experimental Verification', **247**(4), 683-702, (2001).

[9] Y. I. Bobrovnitskii, Journal of Sound and Vibration, 'Estimating the Vibrational Energy Characteristics of an Elastic Structure via the Input Impedance and Mobility', **217**(2), 351-386, (1998).

[10] S. Kim, A. Inoue and R. Singh, SAE Noise and Vibration Conference, 'Experimental Study of Structure-Borne Noise Transfer Paths over the Mid-Frequency Regime', Paper # 05NVC-68, (2005).